ECTI Transactions on Computer and Information Technology
Journal homepage: https://ph01.tci-thaijo.org/index.php/ecticit/
Published by the ECTI Association, Thailand, ISSN: 2286-9131

Comparative Analysis of GLCM Features for ALL Detection using Convolutional Neural Networks

Buntueng Yana[1], Ratsada Praphasawat[2] and Sitthichat Meekhwan[3]

ABSTRACT

Acute Lymphocytic Leukemia (ALL) is the most prevalent childhood cancer. Early diagnosis of ALL is essential, since timely and appropriate therapy significantly improves survival rates. ALL entails abnormal white blood cell (WBC) proliferation that weakens the immune system. Despite numerous studies on ALL identification using microscopic blood smear images, challenges remain due to the structural complexity of blood cells, image noise, intensity inhomogeneity, and cell overlap. Deep learning techniques, particularly CNNs, have shown high efficacy in medical image analysis. However, some studies employ GLCM features that lack an empirical basis for their selection. The study aims systematically evaluate nine distinct GLCM features to provide evidence-based reference for their use in ALL detection. Foundational CNN architecture was used as a classifier to establish a performance baseline with raw color images. Then we compared the baseline to models enhanced with each of the nine GLCM features using the public C-NMC 2019 dataset. The results revealed that GLCM Dissimilarity was the most effective feature, yielding an accuracy of 94.37% and an F1-score of 0.9437. The GLCM Dissimilarity significantly outperformed other GLCM features, followed by GLCM Entropy (93.84%), GLCM Mean (93.57%), GLCM Contrast (93.55%), GLCM Standard Deviation (93.13%), and GLCM ASM (90.98%). A model using only color images achieves an accuracy of 90.53%. It is important to note that although several GLCM features improved performance, among the nine features evaluated, those not listed among the top performers achieved lower accuracy than the color image baseline, highlighting the importance of careful feature selection. These results indicate that specific GLCM features, particularly GLCM Dissimilarity, can substantially enhance CNN-based ALL classification, underscoring its potential as a robust image descriptor for diagnostic applications.

Article information:

Keywords: Acute Lymphocytic Leukemia, Gray Level Co-Occurrence Matrix, Convolutional Neural Network

Article history:
Received: June 19, 2025
Revised: October 9, 2025
Accepted: October 25, 2025
Published: October 31, 2025
(Online)

DOI: 10.37936/ecti-cit.2025194.262809

1. INTRODUCTION

Leukemia is a hematologic malignancy characterized by the abnormal proliferation of blood cells. Diagnosis typically involves blood tests to assess levels of red blood cells, WBCs, and platelets, along with microscopic examination of blood smears. The disease primarily disrupts WBC proliferation, resulting in the overproduction of abnormal WBCs and consequent impairment of immune function.

Leukemia is broadly classified into four principal subtypes: ALL, acute myeloid leukemia (AML), chronic lymphocytic leukemia, and chronic myeloid leukemia. Among these, ALL is the most common childhood leukemia [1], contributing to thousands of deaths in children and adolescents annually. In 2020, there were 57,377 diagnosed cases of ALL worldwide, with almost 55% in the Asia-Pacific region, and 21.9% of these cases involved children. Crucially, early de-

---

[1,3] The authors are with the Department of Electrical Engineering, School of Engineering, University of Phayao, Thailand, Email: mr.buntueng@gmail.com and mr.sitthichat.n@gmail.com

[2] The author is with the Department of Pathology, School of Medicine, University of Phayao, Thailand, Email: ratsada.pr@up.ac.th

[2] Corresponding author: ratsada.pr@up.ac.th

tection of ALL can elevate the survival rates to as high as 90% [2].

ALL is characterized by malignant conversion of lymphoid progenitors and subsequent clonal expansion of lymphoblasts in the bone marrow [3]. This overproduction of lymphoblasts displaces normal blood cell production and severely degrades the immune system [3], which can be fatal if left untreated. The French-American-British (FAB) classification system [3] divides ALL into three main subtypes (L1, L2, and L3) based on cellular morphology. However, intrinsic heterogeneity and subtle morphological variations in microscopic images render automated, accurate classification of ALL challenging.

In the current era of artificial intelligence, computational methods and deep learning techniques are being used for ALL identification using blood smear microscopic images. For instance, various studies [4-7] have demonstrated the application of artificial intelligence in ALL classification. Most studies employ deep learning approaches, which typically require large datasets and substantial computational resources. Deep learning models consist of multiple layers of neural networks designed to automatically extract and learn complex, hierarchical patterns from input data. CNNs are a class of deep learning architectures well suited to image analysis, including detection and recognition tasks. Moreover, CNNs are widely used as backbone feature extractors, capturing discriminative image representations in complex deep learning pipelines.

This research systematically evaluates nine distinct GLCM features to provide an evidence-based reference for their application in CNN-based ALL detection. We focus on a comparative analysis of the GLCM features when integrated with a CNN model for ALL classification. This contribution matters because arbitrary choices of GLCM features in deep learning pipelines can degrade model performance. We address a critical gap in the existing methodology by empirically quantifying the efficacy of individual features. The primary objective of the experiments is to identify which specific GLCM features yield the highest classification accuracy and the lowest loss when utilized with the CNN model, rather than solely aiming to develop a state-of-the-art high-accuracy model for ALL classification. We study how different GLCM features perform in comparison to, and potentially in conjunction with, an RGB image while maintaining a consistent CNN architecture. The goal is to rigorously analyse the performance of these distinct GLCM features to determine their relative effectiveness and potential for enhancing CNN-based ALL classification. By identifying the superior performance of GLCM Dissimilarity, our work directly advances ALL detection research by providing a validated, high-impact feature that improves diagnostic accuracy and guides the intelligent design of next-generation AI models.

2. RELATED LITERATURE

Deep learning techniques have achieved remarkable performance, leading to their widespread adoption in recent medical image analysis. The field of medical image analysis has seen profound advancements through the application of deep learning architectures, notably CNNs, Recurrent Neural Networks (RNNs), and Autoencoders [8]. Among these, CNN-based models are the most frequently employed for image-related tasks. A common challenge is that classical CNNs typically require extensive datasets for practical training and to achieve high performance. To address this data dependency, researchers have explored multiple mitigation strategies, including leveraging transfer learning via pre-trained deep CNN models and proposing novel custom architectures [4].

Current research indicates that artificial intelligence methods for medical image classification are broadly categorized into two primary approaches. The first approach leverages transfer learning, a technique where knowledge from a model pre-trained on a large dataset is adapted for specific tasks, such as ALL classification. The second approach focuses on creating deep learning models from scratch, training them exclusively on the target dataset without relying on pre-trained weights.

The subsequent subsections delve into transfer learning and learning from scratch techniques, specifically in the context of ALL classification. Additionally, this review will discuss commonly used public datasets and examine some of the typical image features that are deployed in this context.

2.1 Transfer Learning Techniques

The transfer learning technique has emerged as a powerful approach in ALL classification. These techniques utilize pre-trained models and subsequently fine-tune their parameters using limited, task-specific datasets. Utilizing pre-trained models is highly effective, even with scarce data, because the weights of the pre-trained layers have already learned robust feature representation from large and diverse datasets. Learned weights are typically partially frozen or updated at a significantly reduced learning rate on the smaller, new dataset. The training process primarily involves updating the weights of the latest output layer and fine-tuning the parameters of a few shallower layers of the pre-trained model. This strategy significantly reduces the training time while often achieving high accuracy with less data. Several prominent transfer learning techniques have been successfully adopted for ALL classification, including established architectures such as You Only Look Once (YOLO) [7-9], MobileNetV2 [4], VGG [10], ResNet [10, 11], EfficientNet [5], alongside custom hybrid models like DL4ALL [12]. These techniques demonstrate the versatility and effectiveness of adapting pre-trained architectures for specific medical diagnostic tasks, such as leukocyte detection and ALL classification [4, 7, 9-11].

In summary, the reviewed literature overwhelmingly supports the effectiveness of transfer learning in ALL classification. The utilization of pre-trained models effectively addresses the challenge of limited medical image data, resulting in both accelerated training times and enhanced classification accuracy. The broad array of architectures and fine-tuning methods discussed highlights transfer learning's significant versatility, cementing its role as a foundational approach for creating powerful diagnostic tools in medical image analysis.

2.2 Learning Techniques From Scratch

Learning from scratch involves the process of designing and training a novel deep learning model entirely from its initial state, bypassing the use of pre-trained models. The entire learning process, from feature extraction to output prediction, relies solely on the dataset provided for the specific task. All model parameters are randomly initialized and then trained exclusively on the target dataset, starting from the initial training epoch. This methodology contrasts directly with transfer learning, where the model is initialized using weights derived from a pre-existing model trained on an benchmark dataset.

Akram *et al.* [13] proposed MIF-Net segmentation of the cytoplasm and nucleus of WBC. The proposed architecture comprises three types of convolutional layers: the standard convolution layer, the strided convolution layer, and the transpose convolution layer. The proposed model was evaluated using four public datasets provided by Jianxi Tecom Science Corporation of China.

Gao *et al.* [1] introduced a Hierarchical Multi-Instance Learning (H-MIL) framework to fully automate childhood leukemia classification based on cytomorphological examination of bone marrow smears. Their framework integrates multi-instance learning with hierarchical classification, enabling training with only patient-level labels and circumventing the need for expensive cell-level annotations. A key innovation is the use of a hierarchical information bottleneck, designed to improve the model's accuracy and generalizability. Performance was evaluated on the CALC dataset, which was collected from the Shanghai Children's Medical Center under ethical approval (SCMCIRB-K2020033-1). This dataset contains the corresponding BM smears and clinical reports from 268 patients. Furthermore, the authors demonstrated the framework's high generalizability on an independent test cohort from a different hospital.

When creating a deep learning model for ALL classification without using pre-trained components, the process generally involves building specialized architectures and training them exclusively on the target dataset. This approach, though less common due to its inherent challenges, provides developers with complete freedom to modify the model's structure as needed. A significant hurdle is the limited availability of large, high-quality medical imaging datasets, which renders the training of complex models from random initialization computationally demanding. However, as demonstrated by specialized designs like MIF-Net and the innovative H-MIL framework, this method offers the distinct advantage of creating highly customized solutions. These solutions are not constrained by the pre-existing biases inherent in models trained on disparate domains, demonstrating that robust performance is achievable when sufficient domain-specific data is available for comprehensive training.

2.3 Publicly Available Datasets

Publicly available datasets for ALL classification are categorized into two types: those containing single cell images and those containing multiple cell images [14]. Single cell images are typically prepared through microscopic preprocessing techniques, such as raw cropping or segmentation. Images derived from raw cropping frequently retain background elements and portions of neighboring cells, while those obtained via segmentation effectively isolate a single cell. Details of the commonly utilized datasets for ALL classification are presented in Table 1.

Table 1: *Publicly available datasets.*

Dataset	Description
ALL-IDB1 [15]	ALL-IDB1 is a multi-cell image dataset designed for developing segmentation and classification algorithms for ALL. It comprises high-resolution images originating from 59 healthy individuals and 49 ALL patients. This dataset comprises individual blood elements, including expert-labeled candidate lymphoblasts, with centroid coordinates provided to facilitate segmentation tasks. Collected by the University of Milan, ALL-IDB1 is notable for its realistic non-uniform background illumination, which presents a challenge requiring robust preprocessing. It has been widely used in research [3, 9, 16-18]
ALL-IDB2 [15]	ALL-IDB2 is a single-cell dataset derived from ALL-IDB1, specifically curated to evaluate classification system performance. It contains 260 cropped images of individual benign and malignant lymphocytes, standardized to 257x257 pixels. By providing pre-segmented and focused images, ALL-IDB2 streamlines classification research, eliminating the need for prior cell

Dataset	Description
	detection or segmentation. It's reduced resolution compared to ALL-IDB1. This dataset has been utilized in prior studies [3, 9, 17, 18].
BCCD	The BCCD dataset is a collection of microscopic images primarily for detecting and classifying blood cell types. It initially holds 364 images, expandable to 875 via augmentation, all at 640x480 pixels. This dataset includes 4,888 labeled objects encompassing WBCs, red blood cells, and platelets. The annotations follow the VOC XML bounding box format. While not exclusively for ALL, its WBC classification utility is crucial for leukemia diagnosis. BCCD, which is publicly available on GitHub and Kaggle, was also integrated by Gan *et al.* [19]. They used it alongside BCDD, PBC, and RaabinWBC to construct the TXL-PBC dataset.
Raabin-WBC[20]	The Raabin-WBC dataset is an extensive, freely available collection of microscopic images intended primarily for the classification of five typical WBC subtypes found in peripheral blood smears. It addresses the need for diverse, labeled hematology data and supports Explainable AI research. The dataset features detailed, double-expert validated labels, encompassing 11 morphological attributes. It offers nucleus and cytoplasm ground truths and exhibits diversity due to data acquisition from various capture devices. Notably, its significant number of lymphocyte images makes it highly relevant for ALL detection, serving as a crucial regular reference. This dataset has been employed in prior research [5].
C-NMC 2019 [21]	The C-NMC 2019 dataset is a high-quality, single-cell image collection of microscopic B-ALL white blood cancer cells from 118 subjects. Designed for the IEEE ISBI 2019 challenge, its primary purpose is to classify normal versus malignant B-ALL cells, with images meticulously labeled for this distinction. The dataset is structured with clear training and testing splits. It is publicly accessible via The Cancer Imaging Archive (TCIA) under a CC BY 3.0 license, with ethical consent obtained for research use. It has been utilized in numerous prior studies [2, 5, 12].

Medical image datasets serve as the cornerstone for the development of artificial intelligence and machine learning models in ALL classification. In this work, we employ the C-NMC 2019 dataset. Further details regarding the C-NMC 2019 dataset and our specific preprocessing methodology are presented in the next section.

2.4 Feature Analysis

Feature extraction is a fundamental and crucial step in image analysis, transforming image data into quantifiable, meaningful representations. These extracted features, which are specific image characteristics or patterns, may be imperceptible to the human eye but are easily recognized and interpreted by algorithms. The effectiveness of these features—their quality, relevance, and discriminative power—directly dictates the accuracy, robustness, and clinical value of subsequent cancer classification and diagnostic systems. Consequently, proficient feature extraction is essential for differentiating subtle pathological changes from normal tissue, thereby enabling precise and reliable cancer diagnosis. The use of texture analysis in blood smear image classification predates deep learning. Earlier research on leukemia detection utilized GLCM features integrated with traditional classifiers including Support Vector Machines (SVMs) and Adaboost [22]. While these studies established the initial utility of GLCM, they often relied on extensive feature engineering and were tested on smaller or older datasets. While many texture descriptors, such as Wavelet[23, 24] and Local Binary Patterns (LBP)[25-28], are used in medical imaging, based on the literature, three texture features widely used in medical imaging include the Gray-Level Run Length Matrix (GLRLM)[29-31], Gray-Level Co-occurrence Matrix (GLCM)[24, 29, 30, 32, 33], and the Gray-Level Size Zone Matrix (GLSZM)[30, 34, 35], are comprehensively presented in Table 2.

Table 2: *Texture features in medical applications.*

Feature	Description
GLRLM	GLRLM describes consecutive pixels with the same gray level within a region of interest. These features are calculated from various matrix types that represent patterns of intensity values and their spatial arrangements. Consequently, these features are instrumental in quantifying the coarseness and fineness of textures. This approach has been studied extensively in medical image applications. Al-Saffar and Yildirim [31] focused on feature extraction for MRI brain classification, specifically deriving grayscale statistical features and GLRLM features from segmented tumor regions. Their experiments showed that the features are effectively identified as a robust, compact set, leading to better classification accuracy and computational efficiency compared to traditional methods. GLRLM features have also been investigated in numerous studies [29, 30].
GLCM	GLCM features are derived from a matrix that quantifies the frequency of pixel pairs possessing specific gray-level values and spatial relationships. t effectively

Feature	Description
	characterizes image texture by capturing properties such as local variations, uniformity, and the linear dependency of pixel intensities. Standard features [32] derived from GLCM include Contrast, Correlation, Homogeneity, Energy, and Entropy. It has been widely applied in medical image analysis [24, 29, 30, 33].
GLSZM	GLSZM is a statistical analysis that quantifies the size of regions formed by continuous pixels sharing the same gray level within an image, thereby constructing an intermediate matrix. The GLSZM captures the size and number of connected regions of pixels that share the same gray level intensity within an image [30]. It provides insight into the distribution of uniform intensity regions, thereby representing the length or size of these connected areas. This feature has been studied in broad fields such as porous media image[34] and breast tomosynthesis[35]

Table 3 summarizes the GLCM features commonly utilized in the surveyed literature. The focus of this study on the GLCM is motivated by its established prominence and proven discriminatory power in medical image analysis. GLCM excels at quantifying the structural complexity and local intensity variations—features essential for distinguishing the fine textural differences between normal and malignant cells in blood smears. Consequently, the subsequent analysis systematically evaluates nine distinct features derived from GLCM. In Table 3, a checkmark signifies that the corresponding feature was utilized in the referenced study; a blank cell indicates that it was not explicitly reported or employed. The column headers employ the following abbreviations for brevity: Ref. for Reference, Con. for GLCM Contrast, Ene. for GLCM Energy, Mea for GLCM Mean, Hom for GLCM Homogeneity, Dis for GLCM Dissimilarity, Cor for GLCM Correlation, Ent for GLCM Entropy, and Var for GLCM Variance.

Table 3: *GLCM features in surveyed literature.*

Ref.	GLCM features							
	Con	Ene	Mea	Hom	Dis	Cor	Ent	Var
[24]	✓	✓	✓	✓				
[36]	✓	✓		✓		✓	✓	
[37]	✓	✓	✓	✓	✓	✓	✓	✓
[22]	✓	✓				✓	✓	

Among the GLCM features, GLCM Contrast and GLCM Energy are the most employed in the reviewed literature. As illustrated in Table 3, these two features are consistently present across almost all surveyed studies, highlighting their robust discriminatory power in medical image analysis. Furthermore, GLCM Homogeneity and GLCM Correlation also appear frequently, indicating their significant role in capturing essential textural information for classification tasks. In this work, we have examined most of the GLCM features in Table 3 and GLCM Angular Second Moment (GLCM ASM). Then we compare the performance of these features with the raw image.

While many existing studies focus on a subset of GLCM features, a comprehensive understanding of their individual efficacy remains lacking. Furthermore, despite the historical integration of GLCM with traditional classifiers [33], a systematic and empirical evaluation of individual GLCM features' effectiveness within a modern Convolutional Neural Network (CNN) architecture was required to establish an evidence-based feature selection guid. To address this, our study extends the analysis to nine distinct GLCM features. Specifically, we selected seven features commonly cited in the literature and summarized in Table 3: GLCM Contrast, GLCM Energy, GLCM Mean, GLCM Homogeneity, GLCM Dissimilarity, GLCM Correlation, and GLCM Entropy. We replaced GLCM Variance with the closely related but more intuitive GLCM Standard Deviation.

Additionally, we included the GLCM ASM. The inclusion of GLCM ASM is motivated by its fundamental representation of image uniformity, and we believe a modern re-evaluation of its utility alongside other features is warranted. This systematic evaluation of nine distinct features aims to provide a complete evidence-based reference for feature selection in this domain.

3. PROPOSED METHODOLOGY

The primary aim of this study is to systematically evaluate and compare the performance of nine distinct GLCM features when applied with a CNN model for ALL classification. This investigation addresses a significant gap in the existing literature, which frequently utilizes GLCM features without providing an empirical basis or clear methodological justification for specific feature selection. By analysing the impact of each feature individually, this work aims to provide an evidence-based reference for feature selection. To facilitate this comparison, we first established a performance baseline by training a CNN model using only the raw images from the dataset. The result from the image-only model serves as our primary point of reference. The experimental workflow conducted in this research is summarized as illustrated in Fig. 1.

The experiments presented in this work were conducted on the publicly available C-NMC 2019 dataset. We utilized PyTorch, a widely used machine learning library, to construct and train our CNN model. The methodology comprises three sequential and interconnected stages for each feature evaluation:

Stage 1 **Data Preparation and Preprocessing:** The C-NMC 2019 images are selected, resized, and augmented to prepare them for subsequent feature extraction and training. Full details of this stage are provided in Section 3.1.

Stage 2 **Feature Extraction:** The specific GLCM features are extracted from the preprocessed images to capture textural information. This process is detailed in Section 3.2.

Stage 3 **CNN Model Development and Evaluation:** The foundation CNN model was designed, and each extracted feature was then individually utilized to train the model, followed by evaluation using ten-fold cross-validation. The architecture, corresponding training parameters, and evaluation methodology are detailed in Section 3.3.

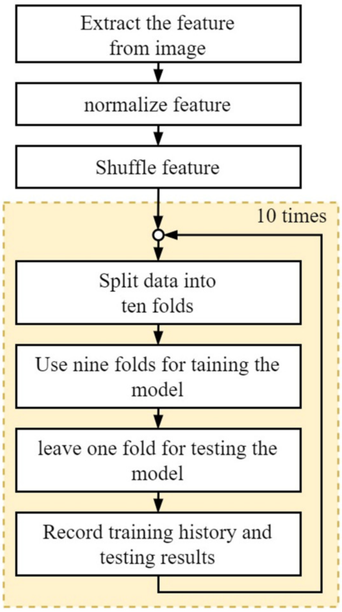

Fig.1: *The proposed methodology for ALL classification.*

The following sections provide a comprehensive overview of the dataset, GLCM features, the model structure, and the performance metrics used in this research.

3.1 C-NMC 2019 dataset

The C-NMC dataset [21] was prepared from bone marrow aspirate slides obtained from both healthy subjects and newly diagnosed B-ALL patients at the Laboratory Oncology Unit, All India Institute of Medical Science (AIIMS), New Delhi, India. This dataset comprises cell images from 118 subjects, including 49 healthy controls and 69 subjects diagnosed with ALL cancer.

For ease of deployment, image sizes were normalized: each cell was centered, and the image was then padded with zero-intensity rows and columns to achieve a uniform size of 450×450 pixels. Subsequently, for the CNN model input, all photos were resized to 350×350 pixels to standardize input dimensions. The images are assigned to two distinct labels: "ALL", representing cells positively diagnosed with Acute Lymphoblastic Leukemia, and "HEM", designating healthy, hematologically normal cells. The ALL group comprises 7,272 images of ALL cells, while the HEM group contains 3,389 images of normal cells.

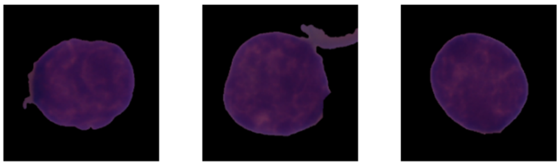

(a) cell images in ALL class

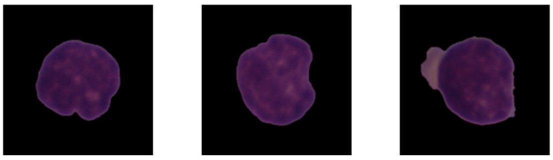

(b) cell images in HEM class

Fig.2: *Exemplars of image in the C-NMC 2019 dataset.*

Illustrative examples of the ALL and HEM cell images can be found in Fig. 2. Each cell image was derived through segmentation from a larger microscopic field-of-view. Subsequently, these cell images were meticulously labelled as either "HEM" or "ALL" class by expert oncologists. Developing high-accuracy learning techniques for this dataset proved challenging due to the inherent variations in the shape and size of ALL cells. To maximize the information available for model training, we utilized all RGB bands. An exemplar illustrating the individual RGB planes is presented in Fig. 3

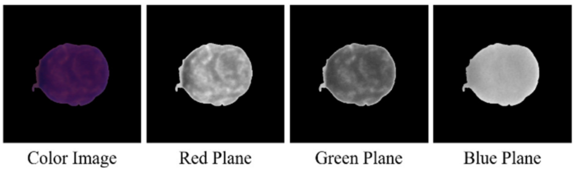

Fig.3: *Color image and the red, green, and blue planes.*

Before being deployed for training or testing in this study, the images required an additional stage of preprocessing. Each image was resized to 350×350 pixels, and the pixel intensity values were normalized within the range of 0 to 1. To address the class imbalance between benign (HEM) and malignant (ALL) images, we applied image augmentation techniques, specifically rotation and mirroring. After this preprocessing, the total number of images in both the HEM and ALL classes was balanced to 7,272 images each, resulting in a total of 14,544 images for our study.

3.2 GLCM features

The GLCM is a statistical method for extracting texture features in image analysis [33, 38]. In this work, GLCM feature extraction is applied independently to each of the three individual color bands of the image. In this work, GLCM feature extraction is applied independently to each of the three individual color bands of the image. Specifically, the GLCM matrix, P(i,j), quantifies the frequency with which a pixel of gray level i and a pixel of gray level j occur together, separated by a defined distance and angle. The resulting matrix forms the basis for computing a set of statistical measures, including Contrast, Dissimilarity, Homogeneity, Energy, and Correlation. These features effectively characterize the underlying texture and structural patterns within an image by capturing properties such as local variations, uniformity, and the linear dependency of pixel intensities. The generation of a spatially descriptive feature map from the color images was achieved through the following two-step process:

1. **Band-wise Extraction:** GLCM feature extraction is applied independently to each of the three individual color bands (red, green, and blue). This information is then consolidated for the CNN input by computing the mean of the GLCM feature maps derived from the three bands, which serves as the final single-channel feature map for training.
2. **Feature Map Generation:** We employ a sliding window technique to transform the global scalar GLCM measures into spatially descriptive feature maps. A local 5×5 window (k=5 in Equation 1) is applied across the entire image. The GLCM matrix is computed within this defined region, and a single GLCM feature value is then derived from the local matrix and assigned to the central pixel, thereby creating a full-resolution GLCM feature map.

Among the measures of spread, this study utilizes explicitly GLCM Standard Deviation rather than GLCM Variance. Although both measures quantify the dispersion of pixel intensities within the co-occurrence matrix, GLCM Standard Deviation is the preferred metric due to its superior interpretability; it expresses data spread in the same units as the original pixel intensity values, offering a more intuitive representation of textural variability.

The mathematical formulations of these key utilized features are detailed in Table 4. The mathematical equations of the GLCM features utilized in this work were slightly modified during implementation to enhance computational speed while preserving the central concept of the standard GLCM features. Specifically, the modifications involved pre-calculating the mean and variance components using Equations (2) to (5) before applying them to the formulas for GLCM Correlation and GLCM Standard Deviation in Table 4. This optimization allows for faster processing of the large image dataset.

Table 4: *Mathematical equations of GLCM features.*

Feature	Mathematical equation
GLCM ASM	$\sum_{i=0}^{N-1}\sum_{j=0}^{N-1} P(i,j)^2$
GLCM Contrast	$\sum_{i=0}^{N-1}\sum_{j=0}^{N-1} P(i,j)(i-j)^2$
GLCM Dissimilarity	$\sum_{i=0}^{N-1}\sum_{j=0}^{N-1} P(i,j)\lvert i-j\rvert$
GLCM Energy	$\sqrt{\sum_{i=0}^{N-1}\sum_{j=0}^{N-1} P(i,j)^2}$
GLCM Entropy	$\sum_{i=0}^{N-1}\sum_{j=0}^{N-1} \tilde{P}(i,j) * \log \tilde{P}(i,j)$
GLCM Homogeneity	$\sum_{i=0}^{N-1}\sum_{j=0}^{N-1} \frac{P(i,j)}{1+(i-j)^2}$
GLCM Correlation	$\sum_{i=0}^{N-1}\sum_{j=0}^{N-1} \frac{(i-\mu_i)(j-\mu_j) * P(i,j)}{\sigma_i * \sigma_j}$
GLCM Mean	$\sum_{i=0}^{N-1}\sum_{j=0}^{N-1} \frac{P(i,j) * i}{N^2}$
GLCM Standard Deviation	$\sqrt{\sum_{i=0}^{N-1}\sum_{j=0}^{N-1} \left(P(i,j) * i - \frac{\mu_i}{N^2}\right)^2}$

When $P(i,j)$ is the normalized GLCM element in row i and column j of the symmetrical GLCM, N is the number of quantized grey levels. In this work, we use $N = 8$. The GLCM is a normalized matrix derived from the raw GLCM counts computed across the local sliding window, as defined by Equation (1). The mean of row (μ_i) and mean of column (μ_j) of GLCM are calculated from equations (2) and (3) respectively. The variance of row i (σ_i) and the variance of column j (σ_j) are computed from Equation (4) and Equation (5), respectively.

$$\tilde{P}(i,j) = \frac{P(i,j)}{\sum_{i=0}^{N-1}\sum_{j=0}^{N-1} P(i,j)} + \frac{1}{k^2} \tag{1}$$

$$\mu_i = \sum_{i=0}^{N-1}\sum_{j=0}^{N-1} P(i,j) * i \tag{2}$$

$$\mu_j = \sum_{i=0}^{N-1}\sum_{j=0}^{N-1} P(i,j) * j \tag{3}$$

$$\sigma_i = \sqrt{\sum_{i=0}^{N-1}\sum_{j=0}^{N-1} (i-\mu_i)^2 P(i,j)} \tag{4}$$

$$\sigma_j = \sqrt{\sum_{i=0}^{N-1}\sum_{j=0}^{N-1} (j-\mu_i)^2 P(i,j)} \tag{5}$$

The window size parameter, denoted by k in Equation (1), is specified as $k = 5$ for our implementation. The utilization of the normalized GLCM element $P(i, j)$ in the Entropy formula (Table 4) is consistent with the standard information-theoretic definition of Entropy, where $P(i, j)$ represents the joint probability of gray-level co-occurrence. This component is added to prevent the GLCM probability $\tilde{P}(i, j)$ from becoming zero, thereby ensuring the logarithm term in GLCM Entropy remains mathematically defined. Thus, the normalization is crucial both for mathematical correctness and computational robustness.

The GLCM features in this work quantify various aspects of texture such as local intensity variations, uniformity, and randomness, providing insights into the visual appearance and structural characteristics of different regions within an image. Additionally, GLCM can derive features like Mean and Standard Deviation to describe the average and spread of pixel intensities in co-occurrence. The source code for the GLCM feature generator was obtained from [39] and was slightly modified to meet the specific requirements of this study. We plot the exemplar of each GLCM feature as illustrated in Fig. 4

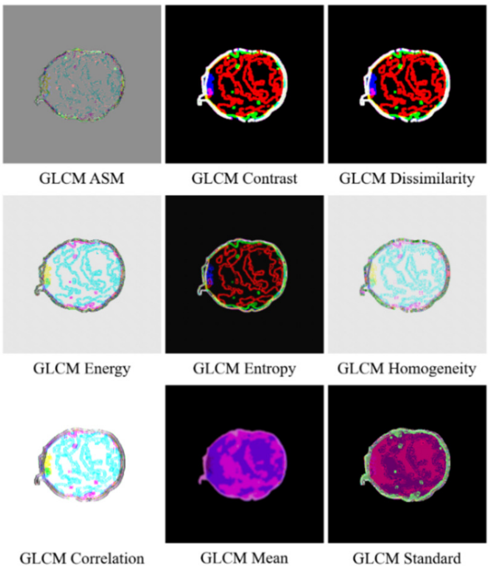

Fig.4: *Exemplar of GLCM feature maps generated using the sliding window technique.*

In this section, we explain the GLCM features, present their mathematical formulations, and visualize exemplars of the GLCM feature maps utilized in this work. For clarity and completeness, the nine specific GLCM features investigated in this study are: GLCM ASM, GLCM Contrast, GLCM Dissimilarity, GLCM Energy, GLCM Entropy, GLCM Homogeneity, GLCM Correlation, GLCM Mean, and GLCM Standard Deviation. These features were selected to provide a broad spectrum of texture descriptors, encompassing measures that range from local variations to those reflecting uniformity and randomness.

3.3 The CNN model

The CNN model utilised in this research comprises several convolutional layers followed by pooling and fully connected layers, as illustrated in Fig. 5. Details of the CNN structure follow,

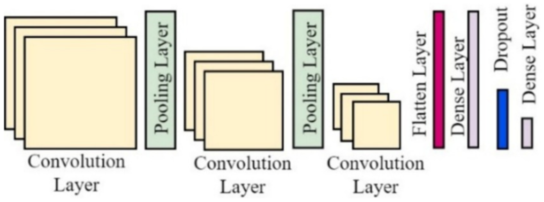

Fig.5: *CNN structure in this work.*

The use of a foundational, scratch-built CNN was a deliberate methodological choice, serving as a neutral and consistent classifier that avoids bias from complex, pre-learned features of models like ResNet or EfficientNet. This design ensures a fair comparison and accurately isolates the intrinsic discriminatory power of each GLCM feature relative to the raw image baseline, thereby addressing the primary objective of this study.

We specifically chose convolutional layers for their efficacy in image classification tasks, as they adeptly extract and learn hierarchical features from input images. The architecture of the CNN model optimises the extraction of relevant image features to achieve high classification accuracy. Pooling layers and Dropout are utilized to reduce the model's complexity and mitigate overfitting. And the model will learn information using a Dense layer. The summary of the CNN structure and trainable parameters has been recorded in Table 5

Table 5: *Summary of the CNN model in this work.*

Layer (type)	Output Shape	Trainable Params
Conv2D	(None, 348, 348, 32)	896
MaxPooling2D	(None, 174, 174, 32)	0
Conv2D	(None, 172, 172, 64)	18,496
MaxPooling2D	(None, 86, 86, 64)	0
Conv2D	(None, 84, 84, 128)	73,856
MaxPooling2D	(None, 42, 42, 128)	0
Flatten	(None, 225792)	0
Dense	(None, 512)	115,606,016
Dropout	(None, 512)	0
Dense	(None,1)	115,669,777

The total number of trainable parameters is 115,699,777. The model was trained using the Adam optimization algorithm and the binary cross-entropy loss function. We used a batch size of 32 and trained each model for 20 epochs, evaluated using a tenfold cross-validation strategy. To provide complete transparency, the training parameters and environment are specified as follows: The Adam optimization algorithm was configured with a learning rate of

1×10^{-4}. The Rectified Linear Unit (ReLU) activation function was consistently employed across all convolutional layers and the first dense layer to introduce non-linearity. The final dense output layer, conversely, utilized the Sigmoid activation function for binary classification. The hardware used for training was an NVIDIA GeForce RTX 3070 GPU and 32 GB of RAM, resulting in an average training time of approximately 4 minutes per epoch. The training and testing data split for each fold is illustrated in Fig. 6.

Fig.6: *Ten-fold cross-validation.*

Following data augmentation, the total number of images in the dataset, encompassing both ALL and HEM labels, is 14,544. The dataset is balanced, comprising 7,272 images for the ALL class and an equal number for the HEM class. We then applied ten-fold cross-validation to evaluate the CNN model rigorously. The process starts with shuffling the images in the dataset. Subsequently, the dataset was partitioned into ten folds. Each fold was used iteratively as the validation set, while the remaining nine folds comprised the training set.

3.4 Performance measurements

We evaluated the performance of the proposed model using the following metrics: accuracy, precision, recall, and the F1-score. The mathematical definitions of these evaluation metrics are presented in Table 6.

Table 6: *Performance measurements.*

Parameters	Mathematical representation
Accuracy	$Accuracy = \frac{T_P + T_N}{T_P + T_N + F_P + F_N}$
Precision	$Precision = \frac{T_P}{T_P + F_P}$
Recall	$Recall = \frac{T_P}{T_P + F_N}$
F1 score	$F1score = \frac{2 \times Precision \times Recall}{Precision + Recall}$

where T_P, T_N, F_P, and F_N are true positive, true negative, false positive, and false negative, respectively.

4. RESULTS AND DISCUSSION

We examined the performance of each feature using ten-fold cross-validation. The average result for each feature is recorded in Table 7. The best accuracy is GLCM Dissimilarity.

Table 7: *Results.*

Feature	Accuracy	Precision	Recall	F1-score
Image	0.9053	0.8958	0.9054	0.9052
ASM	0.9098	0.9241	0.9097	0.9097
Contrast	0.9355	0.9605	0.9354	0.9354
Dissimilarity	0.9437	0.9525	0.9440	0.9437
Energy	0.8440	0.8581	0.8391	0.8079
Entropy	0.9384	0.9567	0.9386	0.9383
Homogeneity	0.8322	0.8499	0.8318	0.7986
Correlation	0.8486	0.8684	0.8461	0.8135
Mean	0.9357	0.9523	0.9357	0.9356
Standard	0.9313	0.9241	0.9097	0.9097

As shown in Table 7, GLCM Dissimilarity demonstrated superior overall performance across all key metrics. GLCM Dissimilarity demonstrated the highest performance among all tested features, achieving peak accuracy (94.37%), F1-score (0.9437), and Recall (0.9440). While GLCM Entropy recorded a slightly higher precision, the robust and balanced performance of GLCM Dissimilarity in the critical metrics of Accuracy and F1-score establishes it as the most effective single GLCM feature for this diagnostic task. This high F1-score specifically confirms the model's balanced capability to accurately identify both positive (ALL) and negative (HEM) cases.

The analysis showed that six specific GLCM features (Dissimilarity, Entropy, Mean, Contrast, Standard Deviation, and ASM) achieved higher classification accuracy than the raw color image input. In the context of clinical diagnosis, the metrics in Table 7 have direct implications for patient care. The primary goal of an automated leukemia detection system is to maximize Recall, as this minimizes the False Negative Rate (FNR), thereby reducing the likelihood of missing an actual ALL case. GLCM Dissimilarity, with the highest Recall of 0.9440, is most effective at reducing the risk of missing a positive diagnosis. Conversely, Precision helps control the False Positive Rate (FP), minimizing unnecessary follow-up procedures.

The clinical application of these findings is to integrate GLCM Dissimilarity-enhanced CNN models into a practical diagnostic workflow as a high-throughput, objective screening tool. This capability would enable pathologists to rapidly filter high-confidence negative (HEM) cases and flag high-risk (ALL) cases, thereby reducing diagnostic fatigue, improving laboratory efficiency, and providing a robust, quantifiable second opinion to support a faster and more reliable diagnosis. Fig. 7 presents a plot of the accuracy results from all experiments. The boxplot on the x-axis illustrates the variation in model accuracy across the multiple cross-validation folds for each specific feature. We acknowledge that a limitation of this study is the exclusive use of the C-NMC 2019 dataset. While this is a high-quality, widely accepted benchmark, the results reflect performance optimized for this dataset's specific characteristics, such as single-cell images, pre-segmentation, and consistent image sizing. Therefore, the generalization of these exact performance metrics to other morphologically distinct datasets, such as ALL-IDB1 or Raabin-WBC, is not guaranteed.

We mitigated potential overfitting by employing extensive image augmentation to balance the classes, complemented by a rigorous ten-fold cross-validation strategy. The consistently high and stable validation accuracy curves for the top-performing GLCM features (Figure 9) further suggest that the model exhibits strong generalization capabilities on unseen data from the same source. For future work, cross-dataset validation, such as testing the GLCM Dissimilarity feature on the ALL-IDB2 dataset, is a necessary step to validate its generalizability as the most robust texture feature for ALL detection.

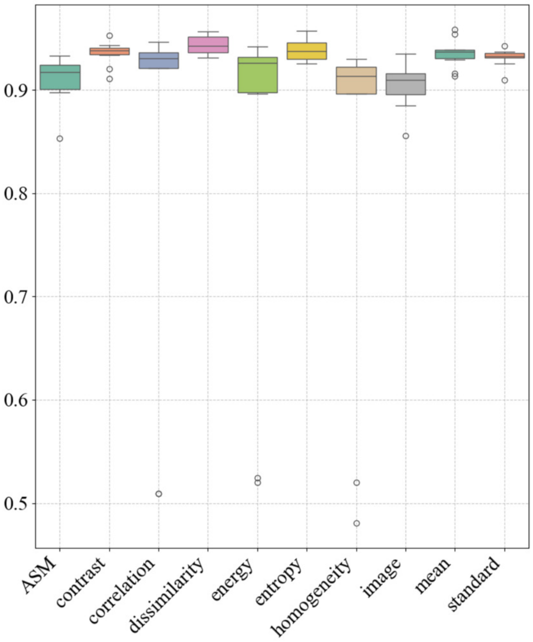

Fig. 7: *The accuracy of GLCM features and colour image.*

From Fig. 7, the overall accuracy of all features is above 90%. The results for the top-performing features—Entropy, Contrast, Dissimilarity, Standard Deviation, Mean, and ASM—exhibit high consistency, thereby demonstrating the model's reliable performance when these features are employed.

For more information, we inspected the training history of the six best performing features to assess the learning ability of the network, as plotted in Fig. 8. The vertical axis of this graph represents the binary cross-entropy loss. The rate of loss decreases and the minimum achieved loss value are direct indicators of the CNN's learning efficiency. From this graph, the training loss of these top GLCM features decreases faster than that of the raw image feature. This trend indicates the model is effectively learning from the training data, as evidenced by the consistent decrease in training loss. Specifically, GLCM Dissimilarity and GLCM Entropy show the fastest convergence and achieve the lowest final loss, confirming that the distinctive textural information is highly effective at guiding the CNN training process.

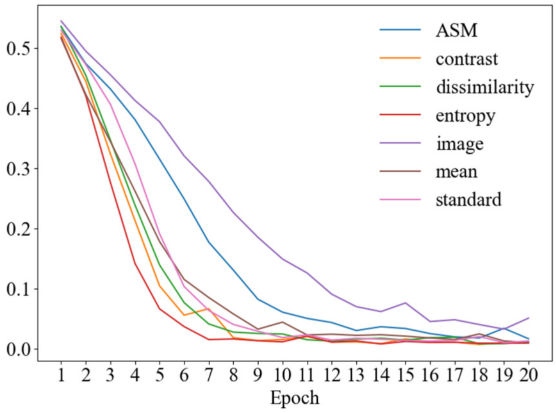

Fig. 8: *Training loss of GLCM features.*

Fig. 9 presents the validation accuracy for the six best-performing GLCM features and the raw image baseline. The vertical axis represents the validation accuracy, a metric that measures the model's generalization performance on unseen data. Higher and more stable final values indicate a more robust model. As depicted in the graph, the GLCM features consistently yield a higher validation accuracy than the raw image baseline.

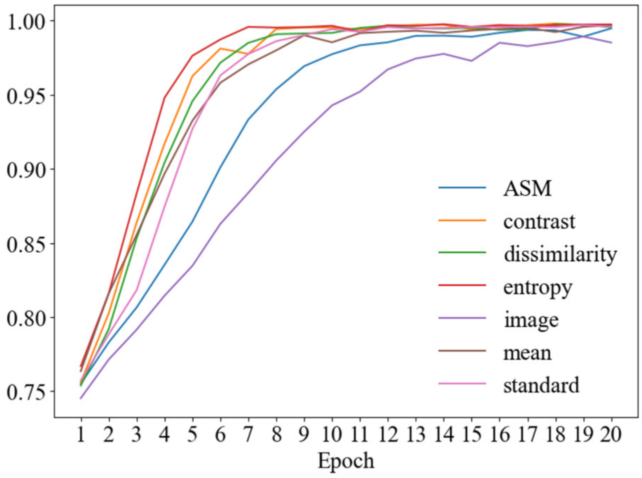

Fig. 9: *Validation accuracy of the experiments.*

This graph confirms that utilizing GLCM features as inputs yields a more robust and accurate model. Specifically, GLCM Entropy and GLCM Dissimilarity achieve the highest validation accuracy, with GLCM Dissimilarity providing the best balance of stability and performance. The models utilizing GLCM features exhibit superior generalization capabilities, achieving higher and more stable validation accuracy compared to the model trained solely on raw images.

This strong performance suggests the model does not overfit significantly to the training data. Furthermore, the model converges relatively quickly, typically within 10 epochs.

5. CONCLUSION

In this work, we systematically studied the performance of GLCM features when applied to ALL classification. Our primary objective was to determine which specific GLCM features are most effective in this diagnostic field, thereby providing an evidence-based reference for feature selection. To achieve this, we utilized a foundational CNN model. We also established a performance baseline by evaluating the raw color image as a reference point.

Our experiments revealed that GLCM Dissimilarity significantly outperformed all other GLCM features in enhancing classification accuracy. This superior performance was followed by GLCM Entropy, GLCM Mean, GLCM Contrast, GLCM Standard Deviation, and GLCM ASM, respectively. All six of these top-performing GLCM features yielded higher accuracy than the raw color image baseline, which achieved an accuracy of 90.53%. This finding demonstrates that well-chosen textural features provide discriminative information that effectively complements the raw pixel data. Conversely, several other GLCM features assessed performed less effectively than the raw color image, underscoring the critical importance of careful feature choice. The models trained with these six best-performing GLCM features consistently demonstrated high accuracy and low loss, exhibiting minimal variability across evaluations. In contrast, GLCM Homogeneity performed the worst among the assessed features, yielding the lowest accuracy and highest loss.

These findings highlight that integrating specific, empirically chosen GLCM features can substantially improve the performance of CNN-based models for ALL classification. The superior performance of GLCM Dissimilarity is particularly noteworthy; as a measure of local intensity variation, its effectiveness suggests that the textural differences between healthy and cancerous cells are a decisive discriminating factor. This result provides a key clinical insight: the subtle yet critical changes in tissue texture—specifically the degree of local intensity change—are more effectively captured by Dissimilarity than by metrics of uniformity or energy. This insight helps focus future feature engineering efforts toward capturing optimal pathological variations. This approach offers a robust method for leveraging textural information to enhance diagnostic accuracy in medical imaging applications.

A potential next step for future work, building upon the identification of GLCM Dissimilarity as the most potent single feature, would be a comprehensive ablation study. Future work could investigate the fusion of multiple top-performing features (e.g., GLCM Dissimilarity and GLCM Entropy) or the concatenation of the best GLCM feature with the raw image data to potentially maximize classification accuracy.

ACKNOWLEDGEMENT

The authors would like to acknowledge the support from the MD68-01 School of Medicine, University of Phayao. This work was also supported by the Thailand Science Research and Innovation Fund and the University of Phayao under Grant No. FF67-UoE225/2567 for the preparation of this manuscript.

AUTHOR CONTRIBUTIONS

Conceptualization, Buntueng Yana and Ratsada Praphasawat; methodology, Buntueng Yana; software, Sitthichat Meekhwan; validation, Buntueng Yana, Ratsada Praphasawat and Sitthichat Meekhwan; formal analysis, Buntueng Yana and Ratsada Praphasawat; investigation, Buntueng Yana; data curation, Sitthichat Meekhwan; writing—original draft preparation, Buntueng Yana; writing—review and editing, Buntueng Yana, Ratsada Praphasawat and Sitthichat Meekhwan; visualization, Buntueng Yana and Sitthichat Meekhwan; supervision, Ratsada Praphasawat; funding acquisition, Ratsada Praphasawat. All authors have read and agreed to the published version of the manuscript.

References

[1] Z. Gao *et al.*, "Childhood Leukemia Classification via Information Bottleneck Enhanced Hierarchical Multi-Instance Learning," in *IEEE Transactions on Medical Imaging*, vol. 42, no. 8, pp. 2348-2359, Aug. 2023.

[2] C. Mondal *et al.*, "Ensemble of Convolutional Neural Networks to diagnose Acute Lymphoblastic Leukemia from microscopic images," *Informatics in Medicine Unlocked*, vol. 27, p. 100794, 2021.

[3] J. Amin *et al.*, "An Integrated Design Based on Dual Thresholding and Features Optimization for White Blood Cells Detection," in *IEEE Access*, vol. 9, pp. 151421-151433, 2021.

[4] P. K. Das and S. Meher, "An efficient deep Convolutional Neural Network based detection and classification of Acute Lymphoblastic Leukemia," *Expert Systems with Applications*, vol. 183, p. 115311, 2021.

[5] A. Batool and Y. -C. Byun, "Lightweight EfficientNetB3 Model Based on Depthwise Separable Convolutions for Enhancing Classification of Leukemia White Blood Cell Images," in *IEEE Access*, vol. 11, pp. 37203-37215, 2023.

[6] M. H. A. M. H. Himel, M. A. M. Hasan, T. Suzuki and J. Shin, "Feature Fusion Based Ensemble of Deep Networks for Acute Leukemia

Diagnosis Using Microscopic Smear Images," in *IEEE Access*, vol. 12, pp. 54758-54771, 2024.

[7] K. Dasaramoole Prakash, J. Khan and K. Kim, "Lightweight and Efficient YOLOv8 With Residual Attention Mechanism for Precise Leukemia Detection and Classification," in *IEEE Access*, vol. 12, pp. 159395-159413, 2024.

[8] J. Redmon, S. Divvala, R. Girshick and A. Farhadi, "You Only Look Once: Unified, Real-Time Object Detection," *2016 IEEE Conference on Computer Vision and Pattern Recognition (CVPR)*, Las Vegas, NV, USA, pp. 779-788, 2016.

[9] M. Sharif *et al.*, "Recognition of Different Types of Leukocytes Using YOLOv2 and Optimized Bag-of-Features," in *IEEE Access*, vol. 8, pp. 167448-167459, 2020.

[10] A. K. Al-Bashir, R. E. Khnouf and L. R. Bany Issa, "Leukemia classification using different CNN-based algorithms-comparative study," *Neural Computing and Applications*, vol. 36, no. 16, pp. 9313-9328, 2024.

[11] P. K. Das, B. Sahoo and S. Meher, "An Efficient Detection and Classification of Acute Leukemia Using Transfer Learning and Orthogonal Softmax Layer-Based Model," in *IEEE/ACM Transactions on Computational Biology and Bioinformatics*, vol. 20, no. 3, pp. 1817-1828, 1 May-June 2023.

[12] A. Genovese, V. Piuri, K. N. Plataniotis and F. Scotti, "DL4ALL: Multi-Task Cross-Dataset Transfer Learning for Acute Lymphoblastic Leukemia Detection," in *IEEE Access*, vol. 11, pp. 65222-65237, 2023.

[13] N. Akram *et al.*, "Exploiting the Multiscale Information Fusion Capabilities for Aiding the Leukemia Diagnosis Through White Blood Cells Segmentation," in *IEEE Access*, vol. 10, pp. 48747-48760, 2022.

[14] T. Mustaqim, C. Fatichah and N. Suciati, "Deep Learning for the Detection of Acute Lymphoblastic Leukemia Subtypes on Microscopic Images: A Systematic Literature Review," in *IEEE Access*, vol. 11, pp. 16108-16127, 2023.

[15] R. D. Labati, V. Piuri and F. Scotti, "All-IDB: The acute lymphoblastic leukemia image database for image processing," *2011 18th IEEE International Conference on Image Processing*, Brussels, Belgium, pp. 2045-2048, 2011.

[16] H. Li, X. Zhao, A. Su, H. Zhang, J. Liu and G. Gu, "Color Space Transformation and Multi-Class Weighted Loss for Adhesive White Blood Cell Segmentation," in *IEEE Access*, vol. 8, pp. 24808-24818, 2020.

[17] Z. Khan *et al.*, "A Framework for Segmentation and Classification of Blood Cells Using Generative Adversarial Networks," in *IEEE Access*, vol. 12, pp. 51995-52015, 2024.

[18] R. Al-Qudah and C. Y. Suen, "Synthetic Blood Smears Generation Using Locality Sensitive Hashing and Deep Neural Networks," in *IEEE Access*, vol. 8, pp. 102530-102539, 2020.

[19] L. Gan, X. Li and X. Wang, "A Curated and Re-annotated Peripheral Blood Cell Dataset Integrating Four Public Resources," *Scientific Data*, vol. 12, no. 1694, pp. 1-12, 2024.

[20] Z. M. Kouzehkanan *et al.*, "Raabin-WBC: a large free access dataset of white blood cells from normal peripheral blood," *bioRxiv*, p. 2021.05.02.442287, 2021.

[21] R. Gupta, S. Gehlot and A. Gupta, "C-NMC: B-lineage acute lymphoblastic leukaemia: A blood cancer dataset," *Medical Engineering & Physics*, vol. 103, p. 103793, 2022.

[22] S. Agaian, M. Madhukar and A. T. Chronopoulos, "Automated Screening System for Acute Myelogenous Leukemia Detection in Blood Microscopic Images," in *IEEE Systems Journal*, vol. 8, no. 3, pp. 995-1004, Sept. 2014.

[23] S. Majumder, A. Paul, F. Schwenker and R. Sarkar, "SAWL-Net: A Statistical Attentions and Wavelet Aided Lightweight Network for Classification of Cancers in Histopathological Images," in *IEEE Transactions on Artificial Intelligence*, vol. 6, no. 8, pp. 2051-2060, Aug. 2025.

[24] M. A. Rejula, B. M. JebIn, R. Selvakumar, S. Amutha and E. George, "Detection of Acute Lymphoblastic Leukemia Using a Novel Bone Marrow Image Segmentation," *Tsinghua Science and Technology*, vol. 30, no. 2, pp. 610-623, 2025.

[25] A. Shah, S. S. Naqvi, K. Naveed, N. Salem, M. A. U. Khan and K. S. Alimgeer, "Automated Diagnosis of Leukemia: A Comprehensive Review," in *IEEE Access*, vol. 9, pp. 132097-132124, 2021.

[26] R. F. Oybek Kizi, T. P. Theodore Armand and H.-C. Kim, "A Review of Deep Learning Techniques for Leukemia Cancer Classification Based on Blood Smear Images," *Applied Biosciences*, vol. 4, no. 1, p. 9, 2025. [Online]. Available: `https://www.mdpi.com/2813-0464/4/1/9`.

[27] P. K. Das, A. Sahu, D. V. A and S. Meher, "SBCDNet: An Efficient Sparse-Based Deep Cascade Blood Cancer Detection Network," in *IEEE Sensors Letters*, vol. 8, no. 1, pp. 1-4, Jan. 2024.

[28] T. A. M. Elhassan, M. S. M. Rahim, T. T. Swee, S. Z. M. Hashim and M. Aljurf, "Feature Extraction of White Blood Cells Using CMYK-Moment Localization and Deep Learning in Acute Myeloid Leukemia Blood Smear Microscopic Images," in *IEEE Access*, vol. 10, pp. 16577-16591, 2022.

[29] M. T. Azam *et al.*, "Optimizing Vertebral Lesion Diagnosis: A CAD-Driven Machine Learning Classification System With Multi-Modal MRI Texture Analysis," in *IEEE Access*, vol. 12, pp.

127846-127861, 2024.

[30] J. Li, D. Zhong, S. Wang, C. Tao and H. Wang, "Analysis of the Influence of CT Imaging Conditions on the CT Image Features of Pulmonary Nodule Phantoms," in *IEEE Access*, vol. 13, pp. 35101-35112, 2025.

[31] Z. A. Al-Saffar and T. Yildirim, "A Novel Approach to Improving Brain Image Classification Using Mutual Information-Accelerated Singular Value Decomposition," in *IEEE Access*, vol. 8, pp. 52575-52587, 2020'

[32] B. A. Varghese, S. Y. Cen, D. H. Hwang and V. A. Duddalwar, "Texture Analysis of Imaging: What Radiologists Need to Know," *American Journal of Roentgenology*, vol. 212, no. 3, pp. 520-528, 2019.

[33] W. Gomez, W. C. A. Pereira and A. F. C. Infantosi, "Analysis of Co-Occurrence Texture Statistics as a Function of Gray-Level Quantization for Classifying Breast Ultrasound," in *IEEE Transactions on Medical Imaging*, vol. 31, no. 10, pp. 1889-1899, Oct. 2012.

[34] A. Singh, K. Regenauer-Lieb, S. D. C. Walsh, R. T. Armstrong, J. J. M. van Griethuysen and P. Mostaghimi, "On Representative Elementary Volumes of Grayscale Micro-CT Images of Porous Media," *Geophysical Research Letters*, vol. 47, no. 15, p. e2020GL088594, 2020.

[35] A. Sakai *et al.*, "A method for the automated classification of benign and malignant masses on digital breast tomosynthesis images using machine learning and radiomic features," *Radiological Physics and Technology*, vol. 13, no. 1, pp. 27-36, 2020.

[36] R. Song, T. Li and Y. Wang, "Mammographic Classification Based on XGBoost and DCNN With Multi Features," in *IEEE Access*, vol. 8, pp. 75011-75021, 2020.

[37] S. Iqbal *et al.*, "Prostate Cancer Detection Using Deep Learning and Traditional Techniques," in *IEEE Access*, vol. 9, pp. 27085-27100, 2021.

[38] R. Anand, T. Shanthi, R. S. Sabeenian, M. E. Paramasivam, and K. Manju, "GLCM Feature-Based Texture Image Classification Using Support Vector Machine," in 3rd EAI International Conference on Big Data Innovation for Sustainable Cognitive Computing, Cham, A. Haldorai, A. Ramu, S. Mohanram, and J. Lu, Eds., 2022// 2022: Springer International Publishing, pp. 143-154.

[39] *GLCM - Fast Gray-Level Co-Occurrence Matrix by numpy.* (2022). GitHub, `https://github.com/tzm030329/GLCM`. Accessed: 2025 January 12.

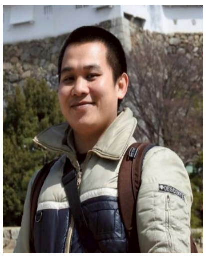

Buntueng Yana is a Lecturer in the Department of Electrical Engineering, Faculty of Engineering, University of Phayao, Thailand, where he has served since 2009. He received his PhD in Information Science and Technology from Osaka University, Japan (2019), and his M.Eng. and B.Eng. in Electrical Engineering from Chiang Mai University, Thailand (2009 and 2006). His expertise includes electronic circuit and embedded-system design, digital communications, wireless networking, artificial intelligence for data analytics, and satellite image processing. Hid research focuses on robotics, machine learning, and automatic control systems.

Ratsada Praphasawat is an Assistant Professor at the School of Medicine, University of Phayao, Thailand. She earned her PhD in Medical Science from Oita University, Japan (2020), an MSc in Pathobiology from Mahidol University, Thailand (2013), and a BSc in Microbiology from Naresuan University, Thailand (2010). Her research focuses on cancer biology and therapeutics, natural product pharmacology, and antimicrobial resistance.

Sitthichat Meekhwan received the bachelor's degree in electrical engineering from the University of Phayao (UP), Phayao, Thailand, in 2019. He is currently studying for a master's degree at the Faculty of Engineering. His current research interests in Machine learning, deep learning, IOT and robotics.